A comparison of jamming behavior in systems composed of dimer- and ellipse-shaped particles†

Carl F. Schreck,[a] Ning Xu[b] and Corey S. O'Hern[ac]

Received 18th January 2010, Accepted 25th March 2010
First published as an Advance Article on the web 17th May 2010
DOI: 10.1039/c001085e

We compare the structural and mechanical properties of static packings composed of frictionless convex (ellipses) and concave (rigid dimers) particles in two dimensions. We employ numerical simulations to generate static packings and measure the shear stress in response to applied simple shear strain as a function of the aspect ratio and amount of compression. We find that the behavior near jamming is significantly different for ellipses and dimers even though both shapes are roughly characterized by the aspect ratio and possess the same number of translational and rotational degrees of freedom per particle. For example, we find that ellipse packings are hypostatic (not isostatic as found for dimers), display novel power-law scaling of the static linear shear modulus and contact number with the amount of compression, and possess stress-strain relations that are qualitatively different from that for dimers. Thus, we observe that important macroscopic properties of static packings of anisotropic particles can depend on the microscale geometrical features of individual particles.

1 Introduction

Significant progress has been made in understanding the jamming transition that occurs in collections of frictionless spherical particles with purely repulsive short-range interactions, where systems transform from liquid- to solid-like states as a function of increasing packing fraction or decreasing applied shear stress.[1–3] Key findings include the power-law scaling of the static shear modulus with packing fraction above the onset of jamming,[4,5] the identification of a growing lengthscale as the system approaches the jamming transition,[6] above which the system can be described as an elastic material,[7] and an abundance of low-energy excitations in the density of vibrational modes.[8] Much of this behavior stems from the fact that frictionless, static packings of spherical particles are typically isostatic since they possess the minimal number of contacts per particle $z_{iso} = 2d$, where d is the spatial dimension, required for mechanical stability.[9]

However, less progress has been made in understanding the jamming transition in particulate systems composed of nonspherical particles, despite the fact that these systems display striking mechanical[10] and rheological[11] properties, and are more relevant for industrial applications and in nature. An important difference between static packings of frictionless spherical *versus* ellipsoidal particles is that the latter are typically hypostatic, not isostatic, with fewer contacts than required to constrain all of the translational and rotational degrees of freedom using straightforward counting arguments, as shown in recent simulations[12–15] and experiments.[16,17] Previous studies have found that for ellipse packings the contact number at jamming $z_J < z_{iso} = 2d_f$, where $d_f = 3$ in two dimensions (2D), over a wide range of aspect ratios α.[12,15] We include similar results from our simulations of static ellipse packings in Fig. 1(a). $z_J < z_{iso}$ for small aspect ratios, but slowly approaches a value z_J^* that is only a few percent below the isostatic value as α increases. In contrast, dimer packings are isostatic with $z_J = z_{iso}$ for all α. However, the packing fraction at jamming ϕ_J, shown in Fig. 1(b), possesses a peak for both ellipses and dimers, which is only a few percent lower than the crystalline value for spherical particles, near $\alpha \sim 1.4$–1.5.[12,17] These results emphasize the point that some structural properties (*e.g.* z_J) of jammed packings are sensitive to microscale geometrical features of individual particles, while others are not (*e.g.* ϕ_J).

2 Motivation

In this manuscript, we investigate the generality of these results for the behavior near jamming of frictionless, anisotropic particles by comparing the structural and mechanical properties of two classes of nonspherical shapes: *convex* (ellipses) and *concave* (rigid dimers) particles. We find that the behavior near jamming for rigid dimers can differ significantly from that for ellipses even

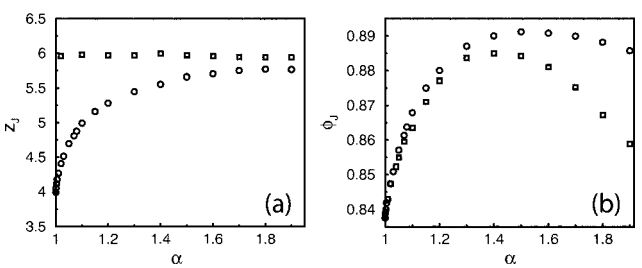

Fig. 1 Ensemble averaged (a) contact number z_J and (b) packing fraction ϕ_J at jamming as a function of aspect ratio α for dimers (squares) and ellipses (circles) for $N = 480$ particles.

[a]*Department of Physics, Yale University, New Haven, CT, 06520-8120, USA*
[b]*Department of Physics, University of Science and Technology, Hefei, 230026, China, USA*
[c]*Department of Mechanical Engineering, Yale University, New Haven, CT, 06520-8286, USA*

† This paper is part of a *Soft Matter* themed issue on Granular and jammed materials. Guest editors: Andrea Liu and Sidney Nagel.

though both shapes are roughly characterized by the aspect ratio and possess the same number of translational and rotational degrees of freedom per particle.

We find several key differences between the structural and mechanical properties of static packings of dimers and ellipses. First, our simulations indicate that static packings of dimers are *isostatic* (not hypostatic as found for ellipses) with $z = z_{iso}$ contacts per particle over the full range of aspect ratios studied as shown in Fig. 1(a). Second, consistent with this, we find that all degrees of freedom are stabilized by quadratic terms in the expansion of the potential energy of the system in small displacements. That is, isostatic dimer packings do not possess quartic vibrational modes as found for hypostatic ellipse packings.[13] Third, ellipse packings display novel power-law scaling of the static linear shear modulus G and contact number $z - z_J$ with $\phi - \phi_J$[13]—both scale linearly with $\phi - \phi_J$. In contrast, for dimer packings G and $z - z_J$ scale as $(\phi - \phi_J)^{0.5}$, which is the same scaling found for static packings of spherical particles.[4] Fourth, we find that the shear stress-strain relations for packings of dimers and ellipses are qualitatively different. For example, at large compressions, the stress response (below the yield stress) to applied strain depends strongly on aspect ratio for ellipses, but it is nearly independent of aspect ratio for dimers. Also, at small compressions, dimer packings display nearly perfect plastic response in a region of strain where sheared ellipse packings possess a growing stress response.

This manuscript is organized as follows. In section 3 we describe the computational methods for generating static packings of ellipses and dimers and then applying quasistatic simple shear to measure the mechanical response. In section 4, we present our results for the linear static shear modulus, contact number, eigenvalues of the dynamical matrix, stress-strain relations, and particle rearrangement statistics. In section 5, we discuss our conclusions and identify possible future research directions to identify the key shape parameters that determine the structural and mechanical properties of static packings of particles with anisotropic shapes. We also include five appendices, which provide the details necessary for calculating the packing fraction for dimers, contact distance between ellipses, and forces, torques, and stress tensor for anisotropic particles.[18]

3 Computational methods

We performed computational studies to measure the structural and mechanical properties of static packings of rigid dimers and ellipse-shaped particles in 2D. The particle shapes we consider are shown in Fig. 2. The rigid dimers are formed by fusing identical disks together. We study aspect ratios $\alpha = a/b$ in the range $1 \leq \alpha \leq 2$, where a and b are the lengths of the major and minor axes, respectively. To inhibit crystallization, we focus on bidisperse mixtures of particles: 2N/3 particles with minor axis b and aspect ratio α, and N/3 larger particles with minor axis 1.4b

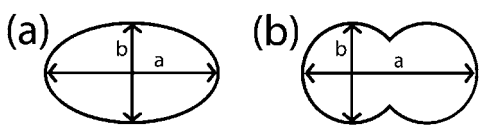

Fig. 2 Definition of the aspect ratio $\alpha = a/b$ (ratio of the major to minor axes) for (a) ellipses and (b) dimers.

and the same α. The particles are enclosed in square simulation cells with box length L and periodic boundary conditions. System sizes were varied from $24 \leq N \leq 480$.

The particles interact *via* soft, pairwise, purely repulsive linear spring potentials. The total potential energy is therefore given by

$$V = \sum_{i>j} V\left(\frac{r_{ij}}{\sigma_{ij}}\right) = \frac{\varepsilon}{2}\sum_{i>j}\left(1 - \frac{r_{ij}}{\sigma_{ij}}\right)^2 \Theta\left(1 - \frac{r_{ij}}{\sigma_{ij}}\right) \quad (1)$$

where r_{ij} is the separation between particles (or monomers) i and j, ε is the characteristic energy scale of the interaction, $\Theta(x)$ is the Heaviside function, and σ_{ij} is the contact distance that in general depends on the orientation of particles i and j, $\hat{\mu}_i$ and $\hat{\mu}_j$, and the direction of the vector $\hat{r}_{ij}$ connecting the centers of particles i and j. For ellipses, $\hat{r}_{ij}$ is along the line connecting the centers of mass of ellipses i and j, while for dimers $\hat{r}_{ij}$ is along the line connecting monomers i and j on distinct dimers k and l.

Contact distance

Determining the interactions between dimers is straightforward: one can identify overlaps between individual disks (monomers) on different dimers. Thus, the contact distance between disk i on a given dimer and disk j on a different dimer is $\sigma_{ij} = (b_i + b_j)/2$, and the total potential energy can be obtained by summing up the contributions $V(r_{ij}/\sigma_{ij})$ over all disk-disk interactions for disks on distinct dimers.

The contact distance σ_{ij} between ellipses is more difficult to calculate than that for dimers. We define σ_{ij} as the distance at which two ellipses will first come into contact when moved along their center-to-center direction while their orientations are held fixed. Fig. 3 illustrates how σ_{ij} is measured for ellipses i and j with orientations $\hat{\mu}_i$ and $\hat{\mu}_j$ at separation vector $\vec{r}_{ij}$. We calculate the contact distances σ_{ij} analytically in systems of bidisperse ellipses using the Perram-Wertheim formulation.[19–22] Further details are provided in Appendix B.

Packing-generation algorithm

We generate static, zero-pressure packings of bidisperse dimers and ellipses using a generalization of the compression/decompression method employed in our previous studies of spherical particles.[23,24] Representative packings of dimers and ellipses at jamming onset are shown in Fig. 4. We briefly outline the packing-generation procedure here for completeness.

We begin the packing-generation process by choosing random initial particle positions and orientations within the simulation

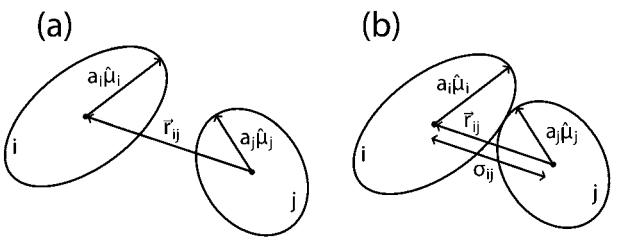

Fig. 3 (a) Ellipses i and j with orientations $\hat{\mu}_i$ and $\hat{\mu}_j$ at center-to-center separation vector $\vec{r}_{ij}$. (b) The contact distance σ_{ij} is obtained by identifying the point of contact when the two ellipses are brought together along $\vec{r}_{ij}$ at fixed orientation.

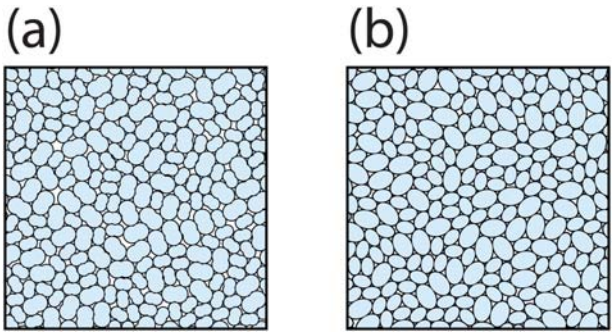

Fig. 4 Snapshots of static packings of $N = 240$ bidisperse (a) rigid dimers ($\phi_J = 0.884$) and (b) ellipses ($\phi_J = 0.892$) with $\alpha = 1.5$ at jamming onset.

cell at packing fraction $\phi_0 = 0.20$ (which is well below the minimum packing fraction at which frictionless packings of ellipses and dimers occur in 2D for $1 \leq \alpha \leq 2$). We successively increase or decrease the minor axes of the particles while maintaining the aspect ratio, with each compression or decompression step followed by conjugate gradient minimization[25] of the total energy (1). The system is decompressed when the total energy at a local minimum is nonzero—*i.e.*, there are finite particle overlaps. If the potential energy of the system is zero and gaps exist between particles, the system is compressed. The increment by which the packing fraction ϕ is changed at each compression or decompression step is gradually decreased. The process is stopped when the total potential energy per particle $V/\varepsilon N \ll 1$. Further details of the packing-generation algorithm are provided in Appendix C.

The packing fraction ϕ_J, contact number z_J, vibrational mode spectrum, and shear stress response to applied shear strain are used to characterize each static packing. The packing-generation process is repeated at least 100 times at each α to generate configurational averages. Once the packings at jamming onset are generated, they can be successively compressed by small amounts $\Delta\phi$, followed by energy minimization at each step, to yield sets of configurations at fixed $\phi - \phi_J$.

Quasistatic simple shear

To determine the mechanical properties of static packings of dimers and ellipses, we studied their response to quasistatic simple shear at fixed area. We first initialized the system with an unsheared packing at a given $\phi - \phi_J$ and successively applied to each particle i small affine simple shear strain steps $\delta\gamma = \delta x/L$ along the x-direction with a gradient in the y-direction:

$$x_i \rightarrow x_i + \delta\gamma y_i \tag{2}$$

where $\vec{r}_i = (x_i, y_i)$ is the location of the center of mass of particle i. To be consistent with simple shear, at each strain step, the angle $\theta_i = \cos^{-1}(\hat{\mu}_i \cdot \hat{x})$ that particle i makes with the x-axis was also rotated:

$$\theta_i \rightarrow \cot^{-1}(\cot\theta_i + \delta\gamma) \tag{3}$$

Each shear strain step was followed by conjugate gradient energy minimization using Lees-Edwards (shear periodic) boundary conditions.[26] For most studies, $\delta\gamma = 10^{-3}$ with accumulated strains $\gamma_t = 1$. We verified that smaller strain steps yielded similar results. During the quasistatic shear, we measured the shear stress (in units of ε/b), contact number, and statistics of particle rearrangement events, which are described in section 4. Details of the calculations of the shear stress for anisotropic particles are provided in Appendices D and E.

4 Results and discussion

We present several measurements of the structural and mechanical properties of static ellipse and dimer packings as a function of aspect ratio and compression $\phi - \phi_J$ including the contact number, vibrational mode spectrum, shear modulus, yield stress, and other features of the shear stress-strain relations.

Contact number at jamming

The contact number is defined by $z = 2N_c/(N - N_r)$, where N_c is the total number of distinct contacts (interparticle overlaps) in the packing. N_r is the number of rattler particles with fewer than three contacts. The contact network is found by identifying all interparticle contacts, and then recursively removing rattler particles until there are none remaining in the packing.

In Fig. 1(a) we show results for the contact number z_J at jamming onset for ellipse and dimer packings. We find that ellipse packings are hypostatic with $z_J < 2d_f$ over the range of aspect ratio $1 \leq \alpha \leq 2$, while dimer packings are isostatic with $z_J \simeq 2d_f$ over the same range of α. The small deviation from isostaticity found in Fig. 1(a) arises from packings where isolated dimers possess only one fully constrained monomer. The unconstrained monomer allows these dimers to freely rotate about the constrained monomer. One can account for these isolated 'rotational' rattler particles and obtain an exact isostatic condition for the contact number.

Vibrational mode spectrum

We showed previously[13,22] that hypostatic packings of ellipsoidal particles possess vibrational modes that are *quartically* (not quadratically) stabilized with the number of quartic modes determined by the deviation from isostaticity, $z_{\mathrm{iso}} - z_J$. In contrast, we expect that all of the nontrivial vibrational modes for dimer packings are quadratically stabilized since dimer packings are isostatic.

To determine the vibrational mode spectrum for each static packing, we calculate the dynamical matrix

$$M_{mn} = \frac{\partial^2 V}{\partial\xi_m \partial\xi_n} \tag{4}$$

where $\xi_m = \{x_m, y_m, a_m\theta_m\}$ and $m, n = 1, \ldots, N$.[27] When (4) is evaluated for each packing and diagonalized using periodic boundary conditions, in principle one obtains $3N' - 2$ nontrivial vibrational eigenmodes, where $N' = N - N_r$. If we assume that all particles have the same mass, the square roots of the eigenvalues of the dynamical matrix give the normal mode frequencies ω_i indexed by i. We denote the normalized eigenvector corresponding to ω_i by $\hat{e}_i = \{e_{x1}^{i=1}, e_{y1}^{i=1}, e_{\theta 1}^{i=1}, \ldots, e_{xi}^{i=N'}, e_{yi}^{i=N'}, e_{\theta i}^{i=N'}\}$ with the constraint that $\hat{e}_i^2 = 1$.

In Fig. 5(a), we show the sorted vibrational mode spectrum for packings of bidisperse dimers and ellipses with $\alpha = 1.1$ and disks ($\alpha = 1.0$) near jamming onset. For disk packings, all of the modes with indexes $1 \leq i/N < 3$ are translational in character, and there are no nontrivial rotational modes. For dimer and ellipse packings at $\alpha = 1.1$, the modes from $0 \leq i/N < 1$ are predominantly rotational and those from $1 \leq i/N < 3$ are predominantly translational in character. The mode spectra for dimer packings display two distinctive features: 1) high-frequency translational modes similar to those for disk packings and 2) rotational modes that are lower in frequency than the translational modes. The mode spectra for the ellipse packings possess a third lower frequency branch that is separated by a gap in frequency from the modes in region 2 as shown in Fig. 5(a).

To determine whether the vibrational modes are quartically or quadratically stabilized at jamming onset, we perturbed the static packings along each of the eigendirections of the dynamical matrix. If $\vec{\xi}_0$ characterizes the centers of mass and orientations of the original static packing, the perturbed configuration obtained after a shift by δ along eigenmode i and relaxation to the nearest local energy minimum is $\vec{\xi}_i = \vec{\xi}_0 + \hat{e}_i$. In Fig. 5(b), we plot the change in the potential energy per particle, $\Delta V_1/N \equiv [V(\vec{\xi}_1) - V(\vec{\xi}_0)]/N$, of the disk, dimer, and ellipse packings in Fig. 5(a) arising from a perturbation along the lowest nontrivial mode as a function of amplitude δ. Fig. 5(b) shows that ΔV_1 scales quadratically with δ for disk and dimer packings. We have also shown that $\Delta V_i \sim \delta^2$ for all higher frequency modes for disk and dimer packings. Thus, static disk and dimer packings possess $2N' - 2$ and $3N' - 2$ quadratic modes, respectively. In contrast, for ellipse packings, $\Delta V_1 \propto \delta^2$ for $\delta < \delta_c$, but $\propto \delta^4$ for $\delta > \delta_c$,[13] where $\delta_c \sim (\phi - \phi_J)^{0.5}$. Thus, static ellipse packings possess vibrational modes that are quartically (not quadratically) stabilized as $\phi \to \phi_J$. We showed previously that the number of quartic modes is determined by $z_{\rm iso} - z_J$.[13]

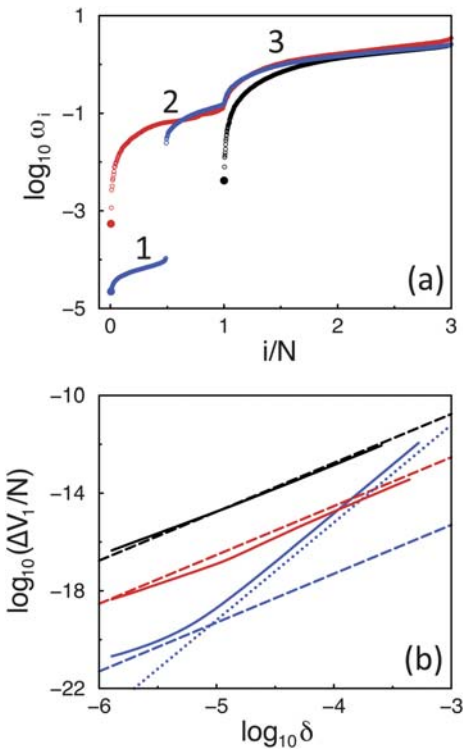

Fig. 5 (a) Sorted vibrational mode spectrum (ω_i *versus* index i/N) for packings of dimers (red) and ellipses (blue) with $\alpha = 1.1$ and disks (black) ($\alpha = 1.0$) near jamming onset. The labels 1, 2, and 3 indicate the translational, quadratic rotational, and quartic rotational mode regions, respectively, as described in the text. (b) Change in potential energy per particle $\Delta V_1/N$ *versus* displacement δ along $\hat{e}_1$ for the lowest nontrivial mode (indicated by the filled circle) for the same disk, dimer, and ellipse packings in (a) (solid lines). $m\omega_1^2\delta^2$ for the lowest mode in each system is also plotted using dashed lines. The dotted blue line has slope 4. For disks and dimers, ΔV_1 is quadratic in δ. In contrast, for ellipses, $\Delta V_1 \propto \delta^2$ for $\delta < \delta_c \sim 10^{-5}$, but $\propto \delta^4$ for $\delta > \delta_c$. The deviations from quadratic behavior at small δ arise from numerical error.

Power-law scaling of linear shear modulus and contact number

One of the hallmarks of the jamming transition in packings of spherical particles is the power-law scaling of the static linear shear modulus G and contact number $z - z_J$ with $\phi - \phi_J$. Both scale as $(\phi - \phi_J)^{0.5}$ for linear repulsive springs, which suggests that the contact number scaling controls the behavior of the linear shear modulus.[4] In Fig. 6, we plot G as a function of $\phi - \phi_J$ for dimers (filled symbols) and ellipses (open symbols) over a range of aspect ratios. We again find power-law scaling near jamming,

$$G = G_0(\alpha)(\phi - \phi_J)^{\beta} \tag{5}$$

where $\beta = 0.5$ and G_0 is weakly dependent on α for dimers. In contrast, $\beta = 1$ for sufficiently small $\phi - \phi_J$ and $G_0(\alpha) \sim (\alpha - 1)^{-0.44\pm0.03}$ for ellipses. The power-law scaling is stronger for ellipse packings, and thus the ratio of the shear moduli $G_{\rm ellipse}/G_{\rm dimer} \to 0$ in the limit $\phi \to \phi_J$ for all α. This implies that ellipse packings are much more susceptible to shear in the linear response regime.

For jammed packings of spherical particles with linear spring interactions both G and $z - z_J$ scale as $(\phi - \phi_J)^{0.5}$. We find similar behavior, $G \sim z - z_J$, for dimer packings as shown in Fig. 7. For ellipse packings, we find

$$z - z_J = z_0(\alpha)(\phi - \phi_J)^{\beta} \tag{6}$$

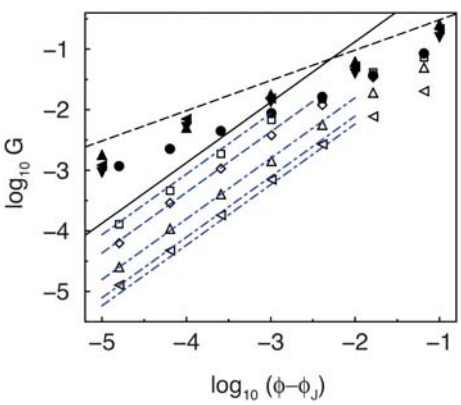

Fig. 6 Static shear modulus G *versus* $\phi - \phi_J$ for $N = 480$ ellipses (open symbols) and 240 dimers (filled symbols) at $\alpha = 1.0$ (circles), 1.002 (squares), 1.01 (diamonds), 1.05 (upward triangles), 1.1 (leftward triangles), 1.5 (downward triangles), and 2.0 (rightward triangles). The solid (dashed) line has slope 1 (0.5). The dot-dashed lines have the form $G = 0.6(\phi - \phi_J)/(\alpha - 1)^{0.44}$.

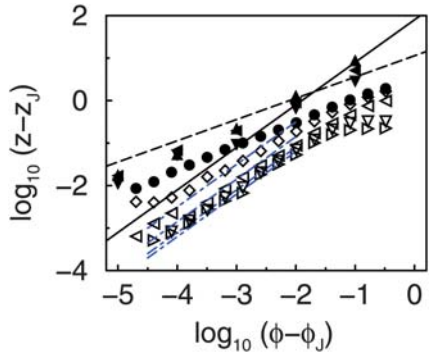

Fig. 7 Deviation in the contact number z from the value at jamming z_J *versus* $\phi - \phi_J$ for $N = 480$ ellipses (open symbols) and 240 dimers (filled symbols) at $\alpha = 1.0$ (circles), 1.002 (squares), 1.01 (diamonds), 1.05 (upward triangles), 1.1 (leftward triangles), 1.5 (downward triangles), and 2.0 (rightward triangles). The solid (dashed) line has slope 1 (0.5). The dot-dashed lines have the form $z - z_J = 6.3(\phi - \phi_J)/(\alpha - 1)^{0.35}$.

where $z_0(\alpha) \sim (\alpha - 1)^{-0.35\pm0.1}$ and $\beta = 1$ for sufficiently small $\phi - \phi_J$. Thus, G and $z - z_J$ have the same power-law scaling with $\phi - \phi_J$ even for hypostatic packings. We showed previously that the novel power-law scaling exponent for G and $z - z_J$ in ellipse packings originates from the quartically stabilized vibrational modes.[13]

Stress-strain relations

The full stress-strain behavior for ellipse and dimer packings is complex; it is qualitatively different for ellipses and dimers and

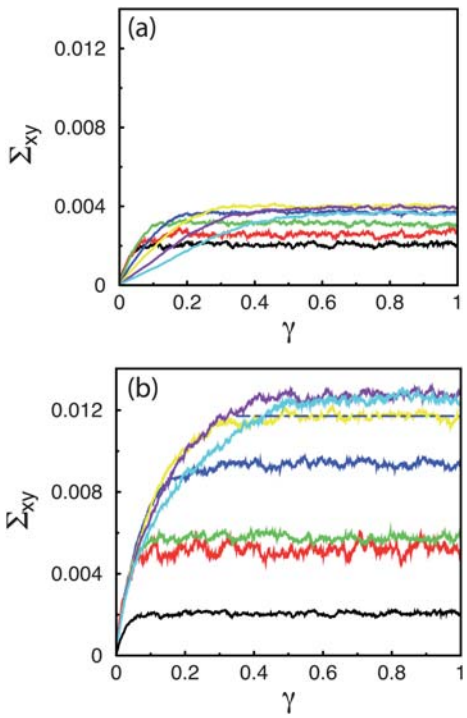

Fig. 8 Shear stress Σ_{xy} *versus* shear strain γ for packings of (a) ellipses and (b) dimers at $\phi - \phi_J = 10^{-1}$ for several aspect ratios $\alpha = 1.0$ (black), 1.05 (red), 1.1 (green), 1.2 (blue), 1.3 (yellow), 1.4 (violet), and 1.5 (cyan). The dashed horizontal line in (b) indicates the yield stress for dimer packings at $\alpha = 1.3$.

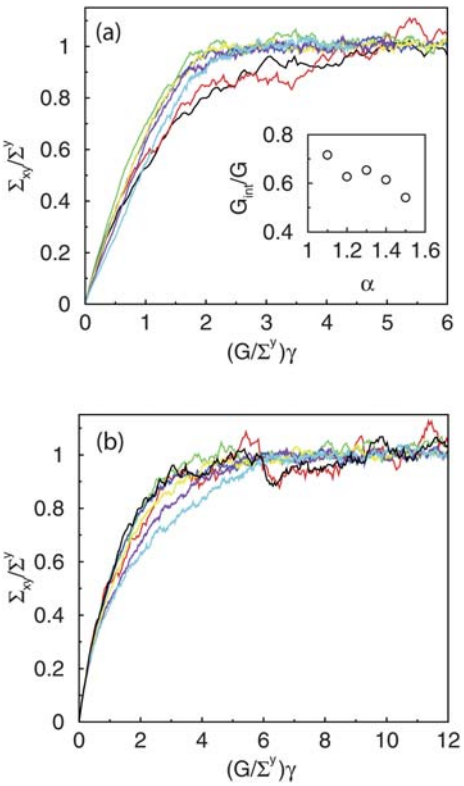

Fig. 9 Same stress-strain relations in Fig. 8 for (a) ellipses and (b) dimers except the shear stress and strain have been scaled by Σ^y and Σ^y/G, respectively. The inset to (a) gives the average value of the slope (G_{int}/G) of the scaled stress-strain relation for shear stresses $\Sigma_{xy} < \Sigma^y$ at aspect ratios $\alpha \geq 1.1$.

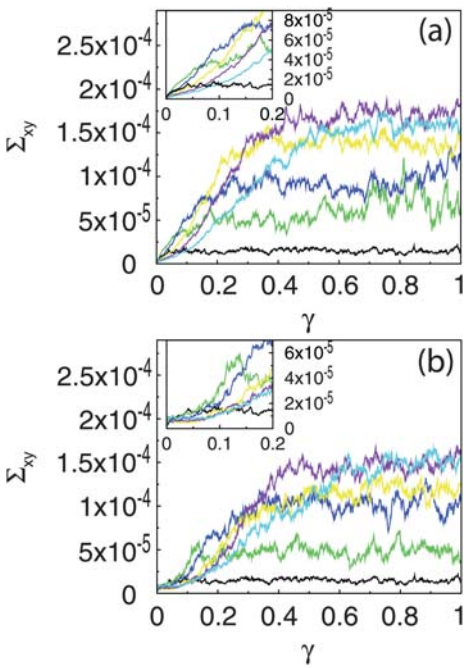

Fig. 10 Shear stress Σ_{xy} *versus* shear strain γ for packings of (a) ellipses and (b) dimers at $\phi - \phi_J = 10^{-3}$ for several aspect ratios $\alpha = 1.0$ (black), 1.1 (green), 1.2 (blue), 1.3 (yellow), 1.4 (violet), and 1.5 (cyan). The insets show the same data as in the main plots, except over a smaller range of γ.

depends nontrivially on $\phi - \phi_J$ and aspect ratio. In Fig. 8 and 10, we show the shear stress Σ_{xy} *versus* strain γ for $\phi - \phi_J = 10^{-1}$ and 10^{-3}, respectively. For ellipses at $\phi - \phi_J = 10^{-1}$ (Fig. 8(a)), the shear stress is roughly linear with strain until the shear stress plateaus at the yield stress, $\Sigma^y = \Sigma_{xy}(\gamma \to \infty)$, which only weakly depends on aspect ratio and is at least a factor of 2 smaller than that for dimers (*cf.* Fig. 14(a)). We can achieve an approximate collapse of the stress-strain data for ellipses at $\phi - \phi_J = 10^{-1}$ for $\alpha \geq 1.1$ by scaling the shear stress by Σ^y and strain by Σ^y/G as shown in Fig. 9(a). The inset to Fig. 9(a) shows that the average shear modulus defined over the wide range $0 \leq \Sigma_{xy} \leq \Sigma^y$ is comparable to the linear response value, G, at small strains (*cf.* Fig. 6) for $\alpha \geq 1.1$.

The behavior of the stress-strain curves for dimers at $\phi - \phi_J = 10^{-1}$ is qualitatively different from that for ellipses as shown in Fig. 8(b). In particular, the approach of the shear stress to the yield stress plateau has significant curvature similar to the behavior found for sheared packings of spherical particles.[28] The scaled stress-strain curve in Fig. 9(b) emphasizes that dimer packings further strain soften as the aspect ratio increases.

Fig. 10 shows the stress-strain behavior for dimers and ellipses much closer to the jamming transition at $\phi - \phi_J = 10^{-3}$. At such small compressions, ellipse packings (Fig. 10(a)) no longer possess such robust, sustained linear response over the full range of shear stress, $0 \leq \Sigma_{xy} \leq \Sigma^y$. Instead, the shear stress is first roughly linear with slope $\sim G$, but then stiffens on approach to the yield stress. However, the most striking feature of the stress-strain curves at $\phi - \phi_J = 10^{-3}$ is the nearly perfect *plastic* response (flat shear stress *versus* strain) for dimer packings (Fig. 10(b)) with $\alpha \geq 1.1$. The plastic regime extends for strains from the end of the linear response regime to $\gamma_p \approx 0.1$. The plastic behavior at intermediate strains is clearly shown in Fig. 11, where we compare the shear stress *versus* strain curves for packings of disks and dimers and ellipses at a single aspect ratio $\alpha = 1.5$. As demonstrated in the inset to Fig. 11, ellipse packings do not possess the nearly plastic response at intermediate strains. In the regime $\gamma < \gamma_p$, for ellipses the shear stress is roughly linear with a shear modulus comparable to G. Furthermore, one can clearly identify the dual behavior of dimers. For small shear strain $\gamma < \gamma_p$, sheared dimer and disk packings behave similarly, while for $\gamma > \gamma_p$, sheared dimer and ellipse packings behave similarly. For $\gamma > \gamma_p$, the shear stress grows rapidly (with positive curvature) as it approaches the yield stress for both ellipses and dimers.

A possible physical mechanism for the plastic behavior at intermediate shear strain is an abundance of particle rearrangements in this strain regime for sheared dimer packings. In Fig. 12, we plot the fraction of particle contacts at strain γ that differ from those at $\gamma = 0$. We find that the plastic behavior in dimer packings is accompanied by a large increase in the number of particle rearrangement events (changes in the contact network) over the shear strain interval $0 \leq \gamma \leq \gamma_p$. Note that the largest fraction (and rate of increase over $0 \leq \gamma \leq \gamma_p$) of particle rearrangements occurs for dimer packings with $\alpha = 1.5$, which possess the most pronounced plastic response. Preliminary studies indicate that the plastic response corresponds to dimers sliding along the shape contours of neighboring dimers, but further work is required to fully elucidate the causative particle-scale motions.

We have also calculated the nematic order parameter, $S = \langle \cos[2(\theta - \theta_0)] \rangle$, where θ_0 is the average orientation of the particles, as a function of shear strain for sheared ellipse and dimer packings as shown in Fig. 13(a) and (b). We find that the nematic order increases with γ up to strains of $\gamma \approx 0.2$–0.3, beyond which it plateaus to a strain independent but aspect ratio dependent value $S_\infty(\alpha)$. In Fig. 13(c), we show that $S_\infty(\alpha)$ grows linearly with α, but shows signs of leveling off near $\alpha^* \approx 1.4$–1.5, which corresponds to the peak in $\phi_J(\alpha)$. In both sheared ellipse and dimer packings, at sufficiently large aspect ratio, the large-strain nematic order is comparable to that in the nematic phase for liquid-crystalline systems.[30] Thus, we have shown that affine simple shear applied to amorphous ellipse and dimer packings can lead to nematic order in 2D for sufficiently large aspect ratio. In future studies, we will explore the robustness of this result by studying boundary driven simple and pure shear in 2D and 3D packings of anisotropic particles.

In Fig. 14, we show the yield stress Σ^y for dimer and ellipse packings as a function of aspect ratio at (a) $\phi - \phi_J = 10^{-1}$, (b) 10^{-2}, and (c) 10^{-3}. We find that the yield stress increases with aspect ratio, which acts as an effective friction coefficient.[30] However, Σ^y begins to level off near $\alpha^* \sim 1.4$–1.5, which is likely related to a maximum in the nematic order near α^*. In contrast to the behavior at small shear strains, the yield stress for dimers and ellipses becomes nearly identical near jamming at $\phi - \phi_J = 10^{-3}$. Thus, measurements of the jamming packing fraction ϕ_J and

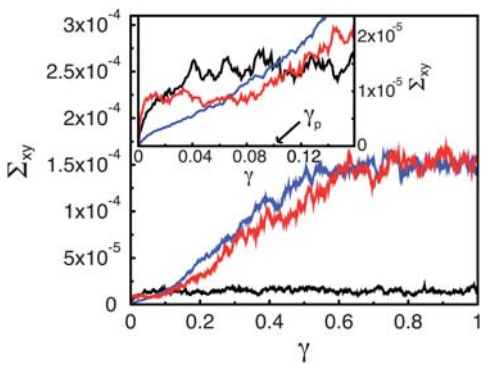

Fig. 11 Shear stress Σ_{xy} *versus* shear strain γ for packings of ellipses (blue) and dimers (red) at $\alpha = 1.5$ and disks (black) at $\phi - \phi_J = 10^{-3}$. The inset shows the same data as in the main plot, except over a smaller range of γ. The end of the intermediate shear strain plastic regime for dimers is indicated by an arrow at $\gamma_p \approx 0.1$.

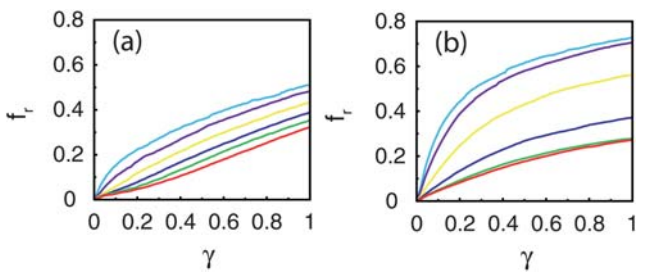

Fig. 12 Fraction f_r of the particle contacts at strain γ that differ from those at $\gamma = 0$ for (a) ellipses and (b) dimers at $\alpha = 1.05$ (red), 1.1 (green), 1.2 (blue), 1.3 (yellow), 1.4 (violet), and 1.5 (cyan).

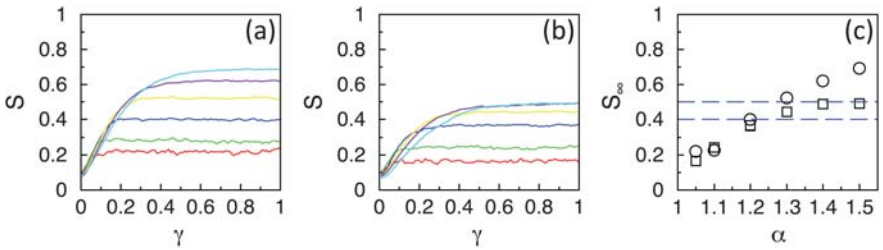

Fig. 13 Nematic order parameter S *versus* shear strain γ for sheared (a) ellipse and (b) dimer packings at $\alpha = 1.05$ (red), 1.1 (green), 1.2 (blue), 1.3 (yellow), 1.4 (violet), and 1.5 (cyan). (c) Large strain limit of the nematic order parameter S_∞ *versus* α for ellipses (circles) and dimers (squares). The dashed horizontal lines at $S_\infty = 0.40$ and 0.50 are typical values of S at which the nematic to isotropic phase transition occurs in quiescent, thermal liquid crystalline systems.

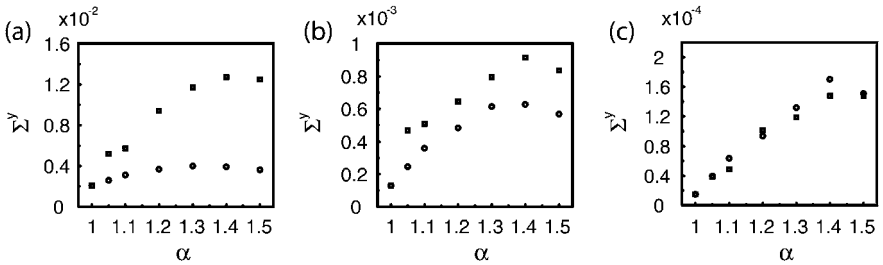

Fig. 14 Yield stress Σ^y as a function of aspect ratio α at (a) $\phi - \phi_J = 10^{-1}$, (b) 10^{-2}, and (c) 10^{-3} for ellipses (circles) and dimers (squares).

yield stress Σ^y are relatively insensitive to microscale geometrical features of individual particles.

5 Future directions

These studies of static and slowly sheared dimer and ellipse packings raise a number of interesting questions that will likely spur new research activity in the area of jamming and glass transitions. For example, we have shown that the structural and mechanical properties of packings of anisotropic particles can depend on the microscale geometric features of individual particles, even those characterized by the same gross shape parameter such as the aspect ratio. To emphasize this point, we studied a single convex particle shape (dimers) and a single concave particle shape (ellipses). We find that the contact number near jamming strongly influences the mechanical properties of the packings. Dimer packings are isostatic with structural and mechanical properties similar to those of disk packings, while ellipse packings are hypostatic, possess $z_{\rm iso} - z_J$ quartic modes, and display novel structural and mechanical properties.

We recognize that the shape comparison of convex *versus* concave particles is likely too broad to capture completely the differences in the mechanical response of packings of anisotropic particles. However, based on our results, we speculate that all packings composed of smooth, nonspherical concave particles will be hypostatic with $z_{\rm iso} - z_J$ quartic modes. Further, we predict that packings composed of the convex particle shapes shown in Fig. 15(a) and (b) will possess qualitatively different mechanical properties. For example, dimers, trimers, and in general n-mers possess notches with radii of curvature $|R_A| < R_B$, where R_B is the radius of each monomer (*i.e.* disk) that comprises the n-mer. We have preliminary results that indicate that n-mers in 2D have $z_J \geq z_{\rm iso}$. In contrast, we expect that static packings composed of peanut-shaped particles[31,32] (*i.e.* those in Fig. 15(b)) will be hypostatic with $z_J < z_{\rm iso}$ because $|R_A| > R_B$, which allows only one contact per notch. Thus, for concave particles, the ratio of the relevant radii of curvature may play an important role in determining the mechanical response of packings.

However, we have also identified structural and mechanical properties that are relatively insensitive to microscale geometric features of anisotropic particles. For example, the jamming packing fraction ϕ_J and yield stress Σ^y, which are thought to

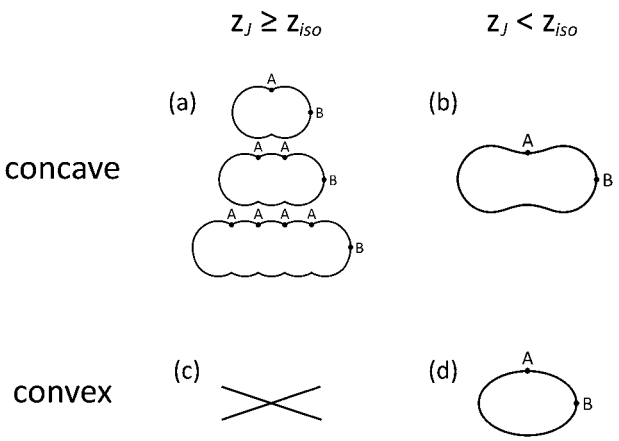

Fig. 15 Examples of smooth, symmetric concave and convex particle shapes. We show two types of concave shapes, (a) dimers, trimers, and in general n-mers with contact number at jamming $z_J \geq z_{\rm iso}$ and (b) peanut-shaped particles with $z_J < z_{\rm iso}$. The key difference between the two types of concave-shaped particles is that the magnitude of the radius of curvature $|R_A|$ at point A in the notch is larger than that at point B, $|R_A| > R_B$, for peanut-shaped particles, while $|R_A| < R_B$ for n-mers. For convex-shaped particles in (d), $R_A > R_B > 0$ and $z_J < z_{\rm iso}$.

control the glass transition in thermalized systems,[33] are very similar for packings of dimers and ellipses with the same aspect ratio (at least over the range of α considered). Thus, a compelling question is whether or not glassy dynamics, caging behavior, and aging are sensitive to microstructural features of anisotropic particles. Thus, we encourage reinvigorated studies of atomic, colloidal, and granular systems to determine under what circumstances geometrical features of individual particles play an important role in jamming behavior and glassy dynamics.

A Packing fraction

In our numerical simulations, we consider bidisperse mixtures of dimers and ellipses in which one-third ($N_l = 1/3$) of the particles are large (with a minor axis 1.4 times that of the smaller particles, *i.e.* $b_l = 1.4b_s$) and two-thirds ($N_s = 2/3$) of the particles are small. When calculating the packing fraction for rigid dimers (fused disks), we do not double count the overlapping region. Thus, we define the packing fraction for dimers in 2D as

$$\phi_{\text{dimer}} = 2N_s\pi\left(\frac{b_s}{L}\right)^2\left(1+\frac{N_l}{N_s}\left(\frac{b_l}{b_s}\right)^2\right)\left(1-\frac{1}{\pi}\left[\cos^{-1}(\alpha-1)+(\alpha-1)\sqrt{\alpha(2-\alpha)}\right]\right) \tag{7}$$

For ellipses

$$\phi_{\text{ellipse}} = N_s\pi\alpha\left(\frac{b_s}{L}\right)^2\left(1+\frac{N_l}{N_s}\left(\frac{b_l}{b_s}\right)^2\right) \tag{8}$$

B Contact distance

The Perram and Wertheim formulation for calculating the contact distance σ_{ij} between ellipses i and j with orientations $\hat{\mu}_i$ and $\hat{\mu}_j$ and center-to-center direction $\hat{r}_{ij}$ involves the following minimization procedure:[20]

$$\begin{aligned}\sigma_{ij} &= \min_\lambda \sigma(\lambda)\\ &= \min_\lambda \frac{\sigma_0(\lambda)}{\sqrt{1-\frac{\chi(\lambda)}{2}\sum_{\pm}\frac{\left(\beta(\lambda)\,\hat{r}_{ij}\cdot\hat{\mu}_i \pm \beta(\lambda)^{-1}\,\hat{r}_{ij}\cdot\hat{\mu}_j\right)^2}{1\pm\chi(\lambda)\hat{\mu}_i\cdot\hat{\mu}_j}}}\end{aligned} \tag{9}$$

where

$$\sigma_0(\lambda) = \frac{1}{2}\left(\frac{b_i^2}{\lambda}+\frac{b_j^2}{1-\lambda}\right)^{1/2} \tag{10}$$

$$\chi(\lambda) = \left(\frac{\left(a_i^2-b_i^2\right)\left(a_j^2-b_j^2\right)}{\left(a_j^2+\frac{1-\lambda}{\lambda}b_i^2\right)\left(a_i^2+\frac{\lambda}{1-\lambda}b_j^2\right)}\right)^{1/2} \tag{11}$$

and

$$\beta(\lambda) = \left(\frac{\left(a_i^2-b_i^2\right)\left(a_j^2+\frac{1-\lambda}{\lambda}b_i^2\right)}{\left(a_j^2-b_j^2\right)\left(a_i^2+\frac{\lambda}{1-\lambda}b_j^2\right)}\right)^{1/4} \tag{12}$$

Determining $\lambda_{\min}$ that minimizes $\sigma(\lambda)$ (eqn (9)) involves solving for the roots of a quartic polynomial in λ for 2D bidisperse systems.[22] The polynomials can be expressed analytically in terms of $\hat{\mu}_i$, $\hat{\mu}_j$, $\hat{r}_{ij}$, and the major and minor axes of particles i and j, and then solved using Newton's method.

C Packing-generation algorithm

In section 3, we outlined our procedure to generate static packings of dimers and ellipses. Here, we provide some of the numerical parameters involved in the simulations. For the energy minimization, we employ the conjugate gradient technique.[25] The two stopping criteria for the energy minimization are $V_t - V_{t-1} < V_{\text{tol}} = 10^{-16}$ and $V_t < V_{\min} = 10^{-16}$, where V_t is the potential energy per particle at iteration t, and the target potential energy per particle of a static packing is $V_{\text{tol}} < V/N < 2V_{\text{tol}}$. For the first compression or decompression step we use the packing-fraction increment $\Delta\phi = 10^{-3}$. Each time the procedure switches from expansion to contraction or *vice versa*, $\Delta\phi$ is reduced by a factor of 2. Using the packing generation procedure with these parameters, we are able to locate the jamming threshold in packing fraction ϕ_J to within 10^{-8} for each static packing.

D Calculation of forces and torques

In this appendix, we provide specific details for calculating the interparticle forces and torques for dimers and ellipses, which are required to perform energy minimization and evaluate the shear stress. The forces and torques can be obtained from the interaction potential (eqn (1)) using generalizations of $\vec{F}_{ij} = dV/d\vec{r}_{ij}$, where $\vec{F}_{ij}$ is the force on particle i due to particle j.

Dimers

For dimers, the interaction force on monomer k_i belonging to dimer i from monomer k_j belonging to a distinct dimer j is

$$\vec{F}_{k_i,k_j} = \frac{dV}{d\vec{r}_{k_i,k_j}} \tag{13}$$

The total force on dimer i is obtained by summing over all monomers k_i belonging to dimer i, all dimers j different from i, and all monomers k_j belonging to dimer j:

$$\vec{F}_i = \sum_{k_i}\sum_{j}\sum_{k_j}\vec{F}_{k_i,k_j} \tag{14}$$

The torque on dimer i arising from an interaction between monomer k_i on dimer i and monomer k_j belonging to dimer j is given by

$$\vec{T}_{k_i,k_j} = \vec{r}_{k_i}\times\vec{F}_{k_i,k_j} \tag{15}$$

where $\vec{r}_{k_i} = d_i(\cos\theta_i\hat{x} - \sin\theta_i\hat{y})$ is the vector from the center of dimer i to the center of monomer k_i, $d_i = b_i(\alpha-1)/2$, and θ_i gives the orientation of dimer i. The total torque on dimer i, $\vec{T}_i$, is obtained by summing $\vec{T}_{k_i,k_j}$ over all monomers k_i on dimer i, all dimers j distinct from i, and all monomers k_j on dimer j.

Ellipses

For ellipses i and j, the interparticle force depends explicitly on how the contact distance σ_{ij} varies with the vector separation $\vec{r}_{ij}$:

$$F_{\xi ij} = -\frac{\partial V}{\partial r_{ij}}\left(\frac{\xi_{ij}}{r_{ij}} - \frac{r_{ij}}{\sigma_{ij}}\frac{\partial \sigma_{ij}}{\partial \xi_{ij}}\right) \tag{16}$$

where $\xi = x, y$. To calculate the torque, one must specify the point of contact. For 'just touching' ellipses i and j are in contact at only one point, as shown in Fig. 16(a), the location $\vec{p}_{ij}$ of the point of contact C_{ij} (relative to the center of mass of ellipse i) is unambiguous and given by

$$\vec{p}_{ij} = p_{ij}^0(\cos(\psi_{ij} + \theta_i)\hat{x} + \sin(\psi_{ij} + \theta_i)\hat{y}) \tag{17}$$

$$p_{ij}^0 = \frac{1}{2\sqrt{\left(\frac{\cos\psi_{ij}}{a_i}\right)^2 + \left(\frac{\sin\psi_{ij}}{b_i}\right)^2}} \tag{18}$$

$$\tan\psi_{ij} = \frac{1}{\alpha^2}\frac{\tan(\Theta_{ij} - \theta_i) - \sigma_{ij}^{-1}\frac{\partial \sigma_{ij}}{\partial \beta_{ij}}}{1 + \sigma_{ij}^{-1}\tan(\Theta_{ij} - \theta_i)\frac{\partial \sigma_{ij}}{\partial \Theta_{ij}}} \tag{19}$$

where $\cos\beta_{ij} = \hat{\mu}_i \cdot \hat{r}_{ij}$, $\cos\Theta_{ij} = \hat{x}_i \cdot \hat{r}_{ij}$. The torque T_{ij} on ellipse i from j is then

$$T_{ij} = p_{xij}F_{yij} - p_{yij}F_{xij} \tag{20}$$

As shown in Fig. 16 (b), upon compression, ellipses are no longer 'just touching', and thus eqn (17) for the point of contact C_{ij} is no longer exact. In this case, we scale $\vec{p}_{ij}$ by r_{ij}/σ_{ij}, which yields an effective point of contact C'_{ij} that is within the overlap region of the two ellipses.

E Calculation of shear stress

For systems composed of spherical particles, the correct form for the stress tensor $\hat{\sigma}_{\alpha\beta}$ in 2D, where $\alpha, \beta = x, y$, is the virial expression:[26]

$$\hat{\Sigma}^V_{\alpha\beta} = \frac{1}{2L^2}\sum_{i>j=1}^{N}\left(F_{ij\alpha}\, r_{ij\beta} + F_{ij\beta}\, r_{ij\alpha}\right) \tag{21}$$

where $F_{ij\alpha}$ is the α-component of the force $\vec{F}_{ij}$ on particle i arising from an overlap with particle j, $r_{ij\beta}$ is the β-component of the vector $\vec{r}_{ij}$ from the center of mass of particle j to that of particle i.

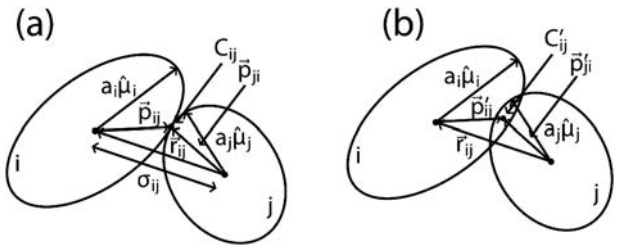

Fig. 16 Definition of the point of contact C_{ij} for ellipses i and j that are (a) 'just touching' and (b) overlapped. $\vec{p}_{ij}$ is location of the point of contact relative to the center of mass of ellipse i. In the overlapped case, the effective point of contact C'_{ij} is given by $\vec{p}'_{ij} = \vec{p}_{ij}(r_{ij}/\sigma_{ij})$.

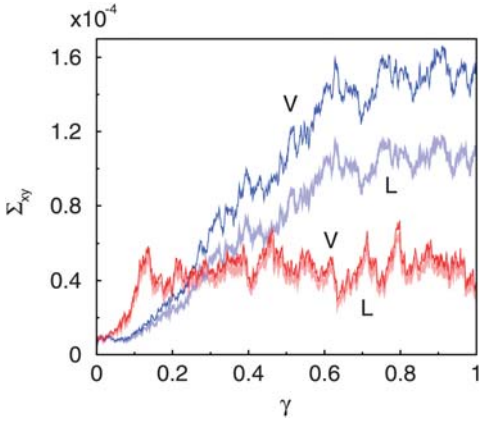

Fig. 17 Comparison of the Love (L) and virial (V) expressions for the shear stress Σ_{xy} as a function of shear strain γ for aspect ratio $\alpha = 1.1$ (red) and 1.5 (blue) at $\phi - \phi_J = 10^{-3}$.

The correct form for the stress tensor $\hat{\sigma}_{\alpha\beta}$ in 2D for systems composed of *anisotropic* particles is the Love expression:[18]

$$\hat{\Sigma}^L_{\alpha\beta} = \frac{1}{2L^2}\sum_{i,j=1}^{N}\left(F_{ij\alpha}\, p_{ij\beta} + F_{ij\beta}\, p_{ij\alpha}\right) \tag{22}$$

where $p_{ij\beta}$ is the β-component of the vector from the center of mass of particle i to the point of contact C_{ij} with particle j. Note that the Love expression reduces to the virial expression for spherical particles.

In our studies of simple shear, we focus on the off-diagonal component of the stress tensor Σ_{xy}. Calculating the point of contact at each shear strain is computationally expensive; we have therefore used the virial expression $\Sigma^V{}_{xy}$ instead of the Love expression $\Sigma^L{}_{xy}$ to quantify the shear stress for both dimer and ellipse packings. As a check, we measured both $\Sigma^L{}_{xy}$ and $\Sigma^V{}_{xy}$ for dimers as a function of aspect ratio and compression. Fig. 17 shows that they give quantitatively similar results for $\alpha = 1.1$ and $\alpha = 1.5$ (for $\gamma < 0.2$), and qualitatively similar results for $\alpha = 1.5$ at large strain. In particular, the plastic response of dimer packings at small compressions is unaffected by the choice of the definition of the shear stress.

Acknowledgements

This work was supported by the National Science Foundation under Grant Nos. CAREER-DMR0448838 and DMS0835742. The authors are grateful to B. Chakraborty, A. Donev, E. Dufresne, M. Mailman, K. Schweizer, and S. Torquato for helpful discussions. This work also benefited from the facilities and staff of the Yale University Faculty of Arts and Sciences High Performance Computing Center and NSF grant no. CNS-0821132 that partially funded acquisition of the computational facilities.

References

1 A. J. Liu and S. R. Nagel, *Nature*, 1998, **396**, 21.
2 Z. Zhang, N. Xu, D. N. Chen, P. Yunker, A. M. Alsayed, K. B. Aptowicz, P. Habdas, A. J. Liu, S. R. Nagel and A. G. Yodh, *Nature*, 2009, **459**, 230.

3 M. van Hecke, *J. Phys.: Condens. Matter*, 2010, **22**, 033101.
4 C. S. O'Hern, L. E. Silbert, A. J. Liu and S. R. Nagel, *Phys. Rev. E: Stat., Nonlinear, Soft Matter Phys.*, 2003, **68**, 011306.
5 W. G. Ellenbroek, E. Somfai, M. van Hecke and W. van Saarloos, *Phys. Rev. Lett.*, 2006, **97**, 258001.
6 L. E. Silbert, A. J. Liu and S. R. Nagel, *Phys. Rev. Lett.*, 2005, **95**, 098301.
7 W. G. Ellenbroek, M. van Hecke and W. van Saarloos, *Phys. Rev. E: Stat., Nonlinear, Soft Matter Phys.*, 2009, **80**, 061307.
8 M. Wyart, S. R. Nagel and T. A. Witten, *Europhys. Lett.*, 2005, **72**, 486.
9 A. V. Tkachenko and T. A. Witten, *Phys. Rev. E: Stat. Phys., Plasmas, Fluids, Relat. Interdiscip. Top.*, 1999, **60**, 687.
10 K. Desmond and S. V. Franklin, *Phys. Rev. E: Stat., Nonlinear, Soft Matter Phys.*, 2006, **73**, 031306.
11 N. Mori, R. Semura and K. Nakamura, *Mol. Cryst. Liq. Cryst.*, 2001, **367**, 445.
12 A. Donev, R. Connelly, F. H. Stillinger and S. Torquato, *Phys. Rev. E: Stat., Nonlinear, Soft Matter Phys.*, 2007, **75**, 051304.
13 M. Mailman, C. F. Schreck, C. S. O'Hern and B. Chakraborty, *Phys. Rev. Lett.*, 2009, **102**, 255501.
14 Z. Zeravcic, N. Xu, A. J. Liu, S. R. Nagel and W. van Saarloos, *Europhys. Lett.*, 2009, **87**, 26001.
15 G. Delaney, D. Weaire, S. Hutzler and S. Murphy, *Philos. Mag. Lett.*, 2005, **85**, 89.
16 W. Man, A. Donev, F. H. Stillinger, M. T. Sullivan, W. B. Russel, D. Heeger, S. Inati, S. Torquato and P. M. Chaikin, *Phys. Rev. Lett.*, 2005, **94**, 198001.
17 A. Donev, I. Cisse, D. Sachs, E. A. Variano, F. H. Stillinger, R. Connelly, S. Torquato and P. M. Chaikin, *Science*, 2004, **303**, 990.
18 S. F. Edwards and D. V. Grinev, *Phys. A*, 2001, **302**, 162.
19 D. J. Cleaver, C. M. Care, M. P. Allen and M. P. Neal, *Phys. Rev. E: Stat. Phys., Plasmas, Fluids, Relat. Interdiscip. Top.*, 1996, **54**, 559.
20 J. W. Perram and M. S. Wertheim, *J. Comput. Phys.*, 1985, **58**, 409.
21 J. W. Perram, J. Rasmussen and E. Praetgaard, *Phys. Rev. E: Stat. Phys., Plasmas, Fluids, Relat. Interdiscip. Top.*, 1996, **54**, 6565.
22 C. F. Schreck and C. S. O'Hern, in *Experimental and computational techniques in soft condensed matter physics*, ed. J. S. Olafsen, Cambridge University Press, London, 2010, ch. 5: Computational methods to study jammed systems.
23 G.-J. Gao, J. Blawzdziewicz and C. S. O'Hern, *Phys. Rev. E: Stat., Nonlinear, Soft Matter Phys.*, 2006, **74**, 061304.
24 G.-J. Gao, J. Blawzdziewicz and C. S. O'Hern, *Phys. Rev. E: Stat., Nonlinear, Soft Matter Phys.*, 2009, **80**, 061303.
25 W. H. Press, B. P. Flannery, S. A. Teukolsky and W. T. Vetterling, *Numerical Recipes in Fortran 77*, Cambridge University Press, New York, 1986.
26 M. P. Allen and D. J. Tildesley, *Numerical Simulations of Liquids*, Oxford University Press, Oxford, 1987.
27 A. Tanguy, J. P. Wittmer, F. Leonforte and J.-L. Barrat, *Phys. Rev. B: Condens. Matter Mater. Phys.*, 2002, **66**, 174205.
28 N. Xu and C. S. O'Hern, *Phys. Rev. E: Stat., Nonlinear, Soft Matter Phys.*, 2006, **73**, 061303.
29 K. Purdy, Z. Dogic, S. Fraden, A. Ruehm, L. Lurio and S. G. J. Mochrie, *Phys. Rev. E: Stat., Nonlinear, Soft Matter Phys.*, 2003, **67**, 031708.
30 L. E. Silbert, D. Ertas, G. S. Grest, T. C. Halsey, D. Levine and S. J. Plimpton, *Phys. Rev. E: Stat., Nonlinear, Soft Matter Phys.*, 2001, **64**, 051302.
31 S. H. Lee, S. J. Gerbode, B. S. John, A. K. Wolfgang, F. A. Escobedo, I. Cohen and C. M. Liddell, *J. Mater. Chem.*, 2008, **18**, 4912.
32 S. J. Gerbode, S. H. Lee, C. M. Liddell and I. Cohen, *Phys. Rev. Lett.*, 2008, **101**, 058302.
33 C. D. Michele, R. Schilling and F. Sciortino, *Phys. Rev. Lett.*, 2007, **98**, 265702.